ADVANCED MATERIALS INTERFACES
Open Access
www.advmatinterfaces.de

Evaluating the Local Bandgap Across $In_xGa_{1-x}As$ Multiple Quantum Wells in a Metamorphic Laser via Low-Loss EELS

Nicholas Stephen, Ivan Pinto-Huguet, Robert Lawrence, Demie Kepaptsoglou, Marc Botifoll, Agnieszka Gocalinska, Enrica Mura, Quentin Ramasse, Emanuele Pelucchi, Jordi Arbiol, and Miryam Arredondo**

Using high-resolution scanning transmission electron microscopy and low-loss electron energy loss spectroscopy, the local bandgap (E_g), indium concentration, and strain distribution across multiple $In_xGa_{1-x}As$ quantum wells (QWs), on a GaAs substrate, within a metamorphic laser structure are correlated. The findings reveal significant inhomogeneities, particularly near the interfaces, for both the indium and strain distribution, and subtle variations in the E_g across individual QWs. The interplay between strain, composition, and E_g is further explored by density functional theory simulations, indicating that variations in the E_g are predominantly influenced by the indium concentration, with strain playing a minor role. The observed local inhomogeneities suggest that differences between individual QWs may affect the collective emission and performance of the final device. This study highlights the importance of spatially resolved analysis in understanding and optimizing the electronic and optical properties for designing next-generation metamorphic lasers with multiple QWs as the active region.

1. Introduction

The integration of metamorphic buffers (MB) into laser structures has greatly advanced the device design and fabrication of semiconductor devices, particularly for telecommunications. Metamorphic lasers incorporate a buffer layer between the substrate and active region to mitigate lattice constant mismatches, facilitating the development of novel laser structures, in which the optoelectronic properties can be enhanced or tuned. Particularly, metamorphic $In_xGa_{1-x}As$ (where x is the mole fraction) quantum well (QW) lasers have demonstrated significant advantages in this regard,[1–4] with multiple QWs (MQWs) offering clear benefits over single QWs, including reduced threshold current,[5] decreased temperature sensitivity[6] and improved quantum efficiency.[7] Moreover, by adjusting the thickness[8,9] and number of QWs,[10] the emission wavelength can be tuned, due to carrier interactions within the laser structure,[11,12] thus enhancing laser performance. However, these performance improvements often assume a certain degree of homogeneity across QWs, a condition heavily influenced by factors such as chemical composition and strain, both governed by the growth conditions.

N. Stephen, M. Arredondo
School of Mathematics and Physics
Queen's University Belfast
University Road, Belfast BT71NN, UK
E-mail: nstephen01@qub.ac.uk; m.arredondo@qub.ac.uk
I. Pinto-Huguet, M. Botifoll, J. Arbiol
CISC and BIST
Catalan Institute of Nanoscience and Nanotechnology (ICN2)
Campus UAB, Bellaterra, Barcelona, Catalonia 08193, Spain
R. Lawrence, D. Kepaptsoglou
School of Physics
Engineering and Technology
University of York
Heslington, York YO10 5DD, UK
The ORCID identification number(s) for the author(s) of this article can be found under https://doi.org/10.1002/admi.202400897

DOI: 10.1002/admi.202400897

D. Kepaptsoglou, Q. Ramasse
SuperSTEM Laboratory
SciTech Daresbury Campus
Daresbury WA4 4AD, UK
A. Gocalinska, E. Mura, E. Pelucchi
Tyndall National Institute
University College Cork
"Lee Maltings", Dyke Parade, Cork T12 R5CP, Ireland
Q. Ramasse
School of Chemical and Process Engineering and School of Physics and Astronomy
University of Leeds
Leeds LS2 9JT, UK
J. Arbiol
ICREA
Pg. Lluis Companys 23, Barcelona, Catalonia 08010, Spain

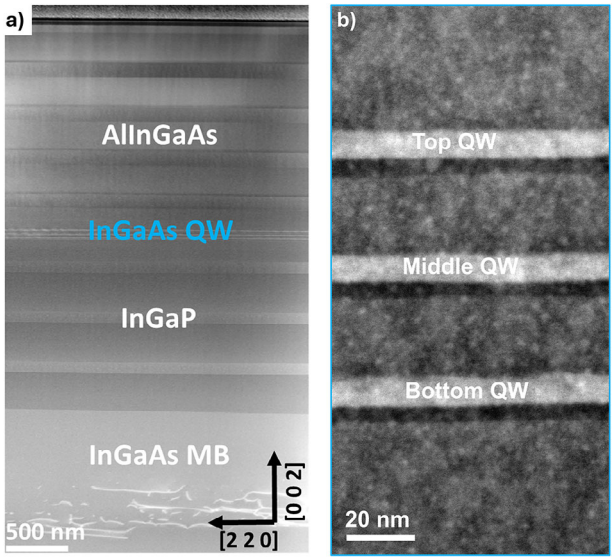

Figure 1. a) ADF-STEM sample overview b) and HAADF-STEM of the $In_{0.40}Ga_{0.60}As$ QWs region.

A key factor in semiconductor laser design is the bandgap energy (E_g), which governs optical transitions and defines the emission wavelength. $In_xGa_{1-x}As$ has a direct E_g, strongly linked to the Indium (In) concentration, allowing laser emissions to be tuned between wavelengths ranging from 1300 to 1550 nm, predominantly used for telecommunication applications.[1,13,14] Importantly, while the bandgap energy dictates the emission wavelength, it is the details of the band structure that critically influence laser performance. Strain, both compressive and tensile, plays a fundamental role in modifying these band structures by altering band edge energies and modifying carrier dynamics.[15–22] Additionally, In concentration also affects the lattice constant,[23] which in turn determines the type and magnitude of strain within the laser's active region and adjacent layers. For example, regions with higher Indium composition experience greater compressive strain. As a result, in addition to controlling the In concentration, strain engineering is important for fine tuning the laser performance. However, the impact of specific In and strain distributions within QWs is still uncertain, mainly due to the limited ability to directly correlate nanoscale variations with changes in the QWs' electronic structure, including E_g. Traditionally, a variety of techniques, including UV–vis spectroscopy,[24] X-ray photoelectron spectroscopy[25] and photoluminescence[26] are used to measure the E_g. While these are effective for bulk materials, they are often limited by the spatial resolution required to capture nanoscale phenomena that occur in thin films and other nanostructures such as QWs and quantum dots (QDs), where heterogeneity in composition, strain, and defects can create localized states within the E_g. In contrast, low-loss electron energy loss spectroscopy (EELS) offers a significant advantage by probing the electronic structure at high spatial resolution with comparable energy resolution to traditional techniques, making it an ideal tool for measuring the E_g at the nanoscale.[27–31] This technique has been applied to a variety of semiconductor materials, including Cu(In, Ga)Se,[32] $In_xGa_{1-x}N$ QWs,[33] CdSe QDs,[27] alpha-alumina grain boundaries,[34] WS_2 nanoflowers[35] and $Mo_xW_{1-x}S_2$ nanoflakes.[36] However, spatially resolved E_g measurements for $In_xGa_{1-x}As$ QWs remain scarce, with most studies focusing on nanostructures, such as InAs/InGaAs nanowires,[37] and few studies examining device structures.[33]

Understanding and controlling local inhomogeneity in QWs within metamorphic lasers is key to advancing technologies in telecommunications, photonics, and beyond, as these directly influence the optoelectronic properties and performance of devices. In this study, we map the In concentration and strain distribution across three stacked $In_{0.40}Ga_{0.60}As$ QWs in an MB laser structure at the nanoscale. Using low-loss EELS, we correlate these spatial variations to the E_g values, providing insight into the complex nanoscale interplay between composition, strain, and bandgap within the QWs. Our findings suggest that variations across individual QWs may significantly impact laser emission, offering valuable insight into designing the next generation of metamorphic lasers with multiple QWs.

2. Results and Discussion

2.1. Structure Overview

Figure 1a is an annular dark field-scanning transmission electron microscopy (ADF-STEM) image displaying a cross-sectional overview of the full metamorphic laser structure, further detailed in Figure S1 (Supporting Information), and elsewhere.[38] The high angle annular dark field (HAADF) STEM image in Figure 1b displays the active region of the metamorphic laser, that containing the MQWs. This region consists of, using nominal thicknesses, a 5 nm GaAs interface controlling layer (CIL), a 7 nm $In_{0.40}Ga_{0.60}As$ QW followed by a 20 nm $In_{0.13}Ga_{0.87}As$ barrier, repeated three times. The measured thickness of all QWs is ≈8.6 nm (Table S1, Supporting Information), with some visible roughness at the interfaces (Figure 1b). For clarity in the next sections, the QW here referred as the bottom QW is that nearest to the $In_xGa_{1-x}As$ MB, while the top QW is that furthest away from the MB.

2.2. In Atomic Fraction Mapping

The relationship between indium (In) concentration and the resulting E_g is well established. Increasing the Indium composition increases the emission wavelength, thereby decreasing the E_g.[39,40] For QWs, the E_g is also intrinsically linked to the dimensions of the confinement, if confined. Thus, controlling the In concentration is a critical parameter in laser design and fabrication, any variations in the composition or thickness of a material such as $In_xGa_{1-x}As$ can alter the band structure, consequently affecting its E_g.

Figure 2 shows the In atomic fraction (at. %) maps across all QWs, acquired by energy dispersive X-ray spectroscopy (EDX) STEM (see Methods). In mole fraction, the QWs' composition is expressed as $In_{0.40}Ga_{0.60}As$, indicating that 50% of the atoms (at. %) are As, 30% are Ga and 20% are In. The relationship between a mole and atomic fraction is further detailed in the Supporting Information. The average In concentration for the bottom, middle

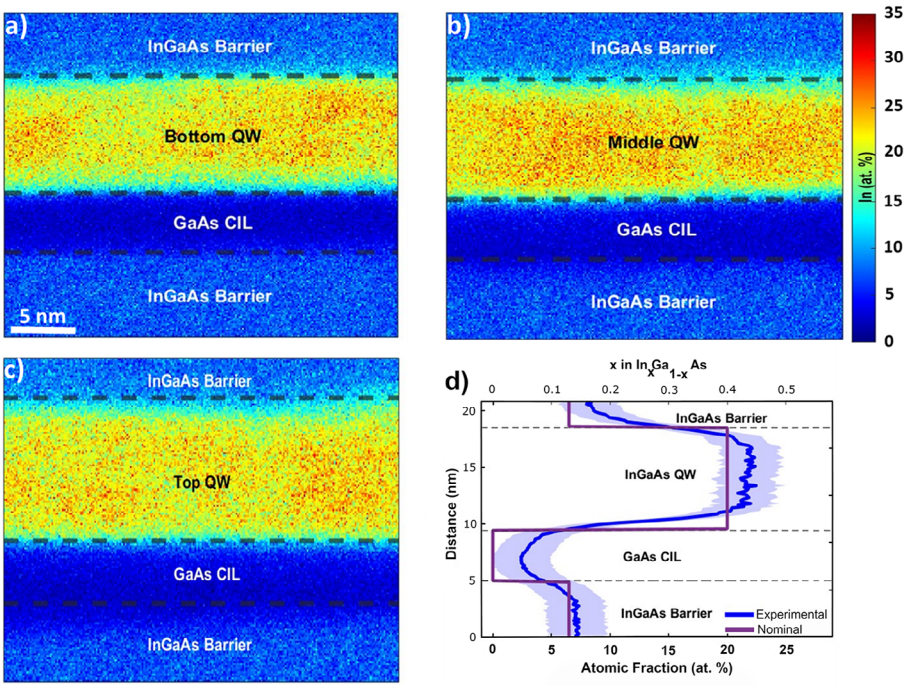

Figure 2. EDX In at. % color map for the a) bottom b), middle c), and top d) QWs region, and representative In at. % profile for the top QW. The blue solid line denotes the experimentally measured In at. % with its uncertainty (shaded area). The secondary *x*-axis indicates x in $In_xGa_{1-x}As$. The pixel size is ≈0.13 nm.

and top QWs are 19.9 ± 4.2 at. %, 21.0 ± 4.1 at. % and 19.7 ± 4.4 at. %, respectively, in agreement with their nominal composition. However, the distribution of In within each QW is not uniform. A significant chemical gradient is observed near the interfaces, for example reaching values as low as ≈15 at. % near the interfaces to ≈22–35 at. % at their centre (Figure 2; Figure S2, Supporting Information). Similar inhomogeneity has been reported for structures containing In: $In_xGa_{1-x}N$[33,41] and $In_xGa_{1-x}As$.[37,42] These variations are significant, as compositional asymmetry has been shown to induce shifts in the E_g.[30,43,44] An In concentration of ≈30 at. % corresponds to a composition of $In_{0.60}Ga_{0.40}As$ and would result in an E_g of ≈0 .68eV. This would represent a decrease of ≈0.2 eV compared to the expected E_g of 0.894 eV for $In_{0.40}Ga_{0.60}As$.[45]

It is worth noting that the chemical composition appears less controllable in lasers grown on metamorphic buffers, likely due to the strain management required on what are overall non-planar surfaces. The surface displays a so-called crosshatched pattern, which may enhance In diffusion during growth.[38] As previously mentioned, variations in the In concentration across the QWs are expected to further impact strain levels, which modifies the lattice parameter and potentially the E_g. Given the strong interplay between composition and strain, we next investigate how the measured In content affects the strain distribution within the QWs.

2.3. Strain Distribution

Strain plays a critical role in modifying the electronic structure of III-V semiconductors, directly influencing the E_g by altering orbital energy levels, demonstrated both theoretically[19,46,47] and experimentally.[48,49] Kuo et al. showed that biaxal tensile strain in $In_xGa_{1-x}As$ epilayers on GaAs (and $In_xGa_{1-x}P$ on InP) leads to a reduction in the E_g, while the opposite effect was observed for compressive strain.[15] Similarly, Gal et al. experimentally demonstrated that for $In_{0.17}Ga_{0.83}As$ QWs the magnitude and sign of strain can be modified as a function of thickness, inducing changes in the E_g.[20] In fact, for certain combinations of strain and QW thickness, the quantum confinement has been demonstrated to further affect the band structure.[17]

In this study, the relative strain along the growth direction ([002], ϵ_{yy}) of the QWs was mapped using geometrical phase analysis (GPA) on the high-resolution annular bright field (ABF) STEM images using reflections g = 004 and g = 2$\bar{2}$0 to minimise strain artifacts at the interfaces[50] (see **Figure 3**; Figure S3, Supporting Information). Geometrical Phase Analysis (GPA) is a Fourier-based image processing method used to measure *relative* strain and deformation in high-resolution TEM and STEM images.[51] ABF-STEM images were chosen over HAADF-STEM images due to the latter's higher sensitivity to surface effects, e.g. surface damage. The $In_{0.13}Ga_{0.87}As$ barrier layer was selected as the reference region due to its homogeneous composition, relatively large size, and close proximity to the QWs. As GPA requires high-resolution images, the field of view is inherently limited, excluding more distant regions such as the metamorphic buffer. The barrier has a lattice constant of 5.706 Å, calculated using Vegard's law and confirmed by EDX (Figure 2d; S2, Supporting Information). Negative strain values indicate tensile strain relative to the reference region, and positive values indicate compressive strain.

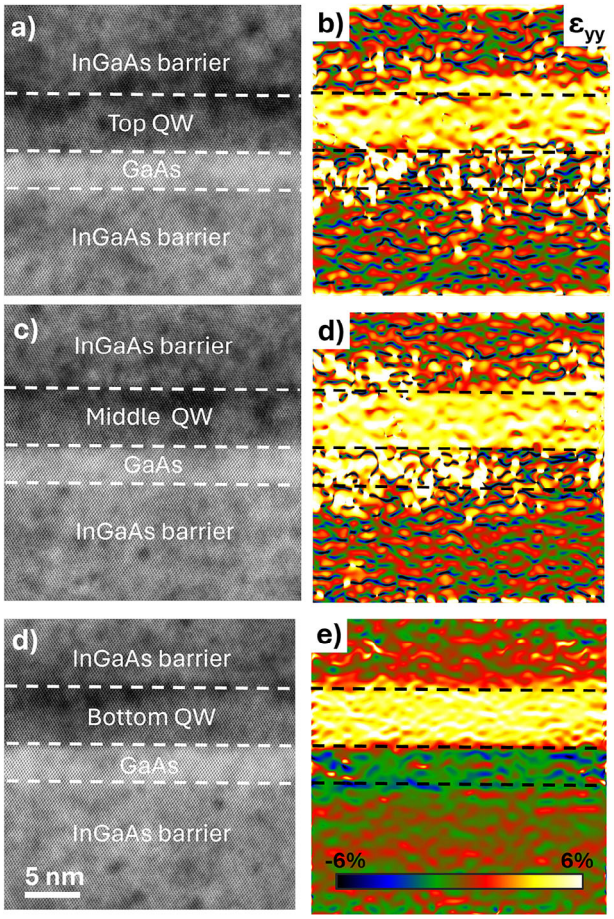

Figure 3. Relative strain distribution across QWs. ABF-STEM viewed down [1 1 0] zone axis image a,c,e) and corresponding ϵ_{yy} strain map b,d,f) for the bottom a,b), middle c,d) and top e,f) QW. Pixel size is 0.039 nm.

In general, the strain varies significantly along the growth direction, while the strain parallel to the interface ([2$\bar{2}$0], ϵ_{xx}) remains largely homogenous (Figure S4, Supporting Information), consistent with previous GPA strain studies on similar metamorphic laser structures.[52] Considering nominal concentrations, the lattice constants for the $In_{0.40}Ga_{0.60}As$ QWs and $In_{0.13}Ga_{0.87}As$ barrier are 5.815 and 5.705 Å, respectively. Typically, the strain for a film grown on a substrate (ϵ) is expressed as:

$$\epsilon = \frac{a_l - a_{ref}}{a_l} \times 100\% \quad (1)$$

where a_l, is the lattice constant of the layer of interest and a_{ref} is the lattice constant of the reference layer. Thus, as per Equation 1, the strain in the QWs is expected to be compressive. Similarly, the GaAs CIL has a smaller lattice constant (5.653Å) than the $In_{0.13}Ga_{0.87}As$ barrier, resulting in tensile strain. The relative strain analysis confirms that the QWs are under compressive strain and the GaAs CIL layer is under tensile strain (Figure 3; Figures S4 and S5, Supporting Information).

The relative strain distribution across the QWs (Figure 3) closely resembles the In concentration profiles (Figure 2), reaching a maximum at the QWs' centers and decreasing near the interfaces, with strain values as high as 4% present at the center of the top QW. This is expected, as regions with higher indium content will experience greater compressive strain. Despite this qualitative agreement, the measured strain values in the QWs deviate from the expected values based solely on the measured In concentration (see Figure S5, Supporting Information). For example, according to Vegard's law, a strain value ≈3.8% would correspond to an In concentration of $In_{0.68}Ga_{0.32}As$, equivalent to 34 at. % In. This estimated concentration is higher than the measured In concentration at this point (22.11 ± 2.86 at. %), and a similar deviation is observed for the other two QWs. These discrepancies suggest that other factors, such as interface effects and surface variations in the lamellae may be influencing the GPA measurements. However, despite these variations, the relative strain distribution qualitatively agrees with the In composition profile.

The next section investigates the variations in E_g across the QWs and explores their relationship to both strain and indium distribution.

2.4. Bandgap Measurements Across Multiple QWs

The optical E_g can be phenomenologically calculated as described by Nahory et al.[45] At 300K, the E_g of $In_xGa_{1-x}As$ can be expressed in terms of the In mole fraction (x), as defined in Equation (2):

$$E_g\ (x) = 1.425eV - x\ 1.501eV + x^2\ 0.436eV \quad (2)$$

For the nominal $In_{0.40}Ga_{0.60}As$ QWs composition, the expected E_g is 0 .894eV. While this equation does not consider the QW thickness, known to affect the E_g in $In_xGa_{1-x}As$ QWs,[53] it provides a good approximation given that all QWs are nominally identical. Band bending[54] is not expected to significantly impact the QWs due to the relatively large separation between them within the laser structure, allowing each QW to be considered independently. It is worth noting that Equation (2) does not consider quantum confinement or strain effects. However, this equation is used as a good approximation to compare against the measured trends, and not absolute values.

Low-loss EELS at 60 kV and a probe size of ≈1.4Å was used to measure the E_g across all QWs, see Experimental Section. The spectra were corrected for Cerenkov radiation as described in the Experimental Section and Supporting Information, following the procedure published in ref.[28] The error provided for each E_g is the uncertainty from the fitting procedure. Cerenkov radiation occurs when electrons travel faster than the speed of light in a medium, causing a reduction in the measured E_g.[55,56] **Figure 4b** summarises the spatially resolved and corrected E_g measured across all QWs, from the bottom (position 1) to the top interface (position 6), as indicated by the yellow boxes in Figure 4a and marked by the arrow, with a box size of 173 × 4 pixels (≈15.3 × 0.3 nm). It should be noted that the corrected E_g values follow the same trend as the uncorrected data but are higher (Figures S7, S13 and S14, Supporting Information). Complete E_g profiles of adjacent layers are provided in Figure S9 (Supporting Information). The average E_g values for the QWs are 0.900 ± 0.017 eV for the top QW, 0.923 ± 0.015 eV for the middle QW and 0.883 ± 0.021 eV for the bottom QW (**Figure 5a**). Subtle E_g fluctuations within and between individual QWs are not captured when

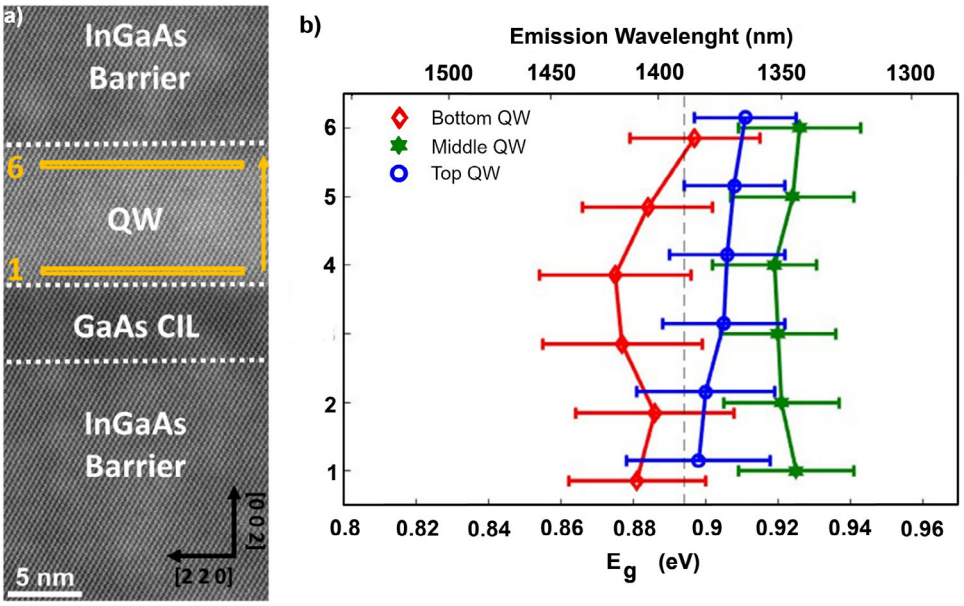

Figure 4. E_g analysis. Representative HAADF-STEM image of the bottom QW, a) and the corresponding measured E_g b) corrected for Cerenkov: bottom (red diamond), middle (green hexagon) and top QW (blue circle). The E_g was measured horizontally as indicated by the yellow markings in (a). The secondary axis shows the corresponding emission wavelength. The dashed gray line represents the calculated E_g for $In_{0.40}Ga_{0.60}As$ from Nahroy et al.[45]

lower resolution EELS is acquired, over all QWs (Figure S10, Supporting Information), highlighting the importance of spatially resolved measurements.

Considering the average E_g values, and their uncertainties, the highest upper value would be 0.938 eV and the lowest upper value 0.862, indicating a possible maximum variation of ≈0.076 eV between individual QWs. These values are within the range of the sample's bulk emission measured by photoluminescence (PL)[38] (Figure S11, Supporting Information), which has the main emission peak at ≈1360 nm (E_g = 0.914 eV) with a full-width half maximum extending from 1320 to 1410 nm (E_g = 0.941 eV–0.881 eV). It is plausible that fluctuations in the individual E_g values may contribute to the extended range observed in the PL data. Moreover, subtle spatial variations within the individual QWs are observed, particularly for the bottom QW which exhibits an apparent asymmetry near the interfaces, with the E_g values increasing toward the $In_{0.13}Ga_{0.87}As$ barrier and decreasing toward the bottom GaAs CIL.

The strain is at its lowest near the interfaces, consistent with the Indium composition, and a similar spatial variation would be expected for the E_g. However, surprisingly, only the bottom QW exhibits a slight but asymmetric difference in the calculated E_g values near the interfaces.

Thickness variations in the areas containing the QWs were considered as a potential source of the differences in the measured E_g. However, this effect was neglected after carefully considering the changes in the relative thickness (t/λ) and the measured E_g, see Figure S12 (Supporting Information).

To better understand the observed E_g variations, we consider the composition effect. Figure 5a shows the measured average E_g and In concentration for each QW. All values are near the E_g calculated using Equation (2) (dashed purple line in Figure 5a) and within the PL measurements, demonstrating that the E_g values calculated from low-loss EELS are reasonable. However, as mentioned, subtle variations in the E_g values are evident across individual QWs, particularly within the bottom QW (Figure 5b), where an asymmetry is more apparent, with only the central values falling within the expected range for the measured In concentration, considering uncertainties.

Density Functional Theory (DFT) simulations were conducted to further explore the effects of varying strain and composition on the E_g, and correlate these to the observed trends for the measured E_g. Figure 5c,d presents the simulated low-loss EELS for various $In_xGa_{1-x}As$ alloys under different strains. These simulations consider the strain to be uniaxial (as shown in the Figure 5d inset) and do not account for surface effects or Cerenkov radiation. Moreover, DFT underestimates the onset energy and consequently E_g due to derivative discontinuity.[57,58] The onset energy is the minimum energy loss observed in the spectrum where a distinct increase in intensity occurs and is used to estimate the material's band gap.[59] Despite these limitations, this approach is known for its good reproducibility, making it ideal for identifying trends related to changes in strain and chemical composition.[60,61]

Figure 5c shows the onset energy as a function of x in $In_xGa_{1-x}As$. In general, the simulations indicate that irrespective of the strain regime, the energy onset decreases as the In concentration increases, with the most drastic changes observed for the highest strain magnitudes. For compositions between x = 0.1 and 0.6 the compressive strain exhibits the lowest energy onset values compared to tensile strain. Figure 5d plots the change in the energy onset and the corresponding loss function for the $In_{0.375}Ga_{0.625}As$ composition, close to the QWs nominal composition ($In_{0.40}Ga_{0.60}As$), as a function of strain. Additional plots for other compositions are shown in Figure S15 (Supporting Information) and the band gap bowing effect is shown in

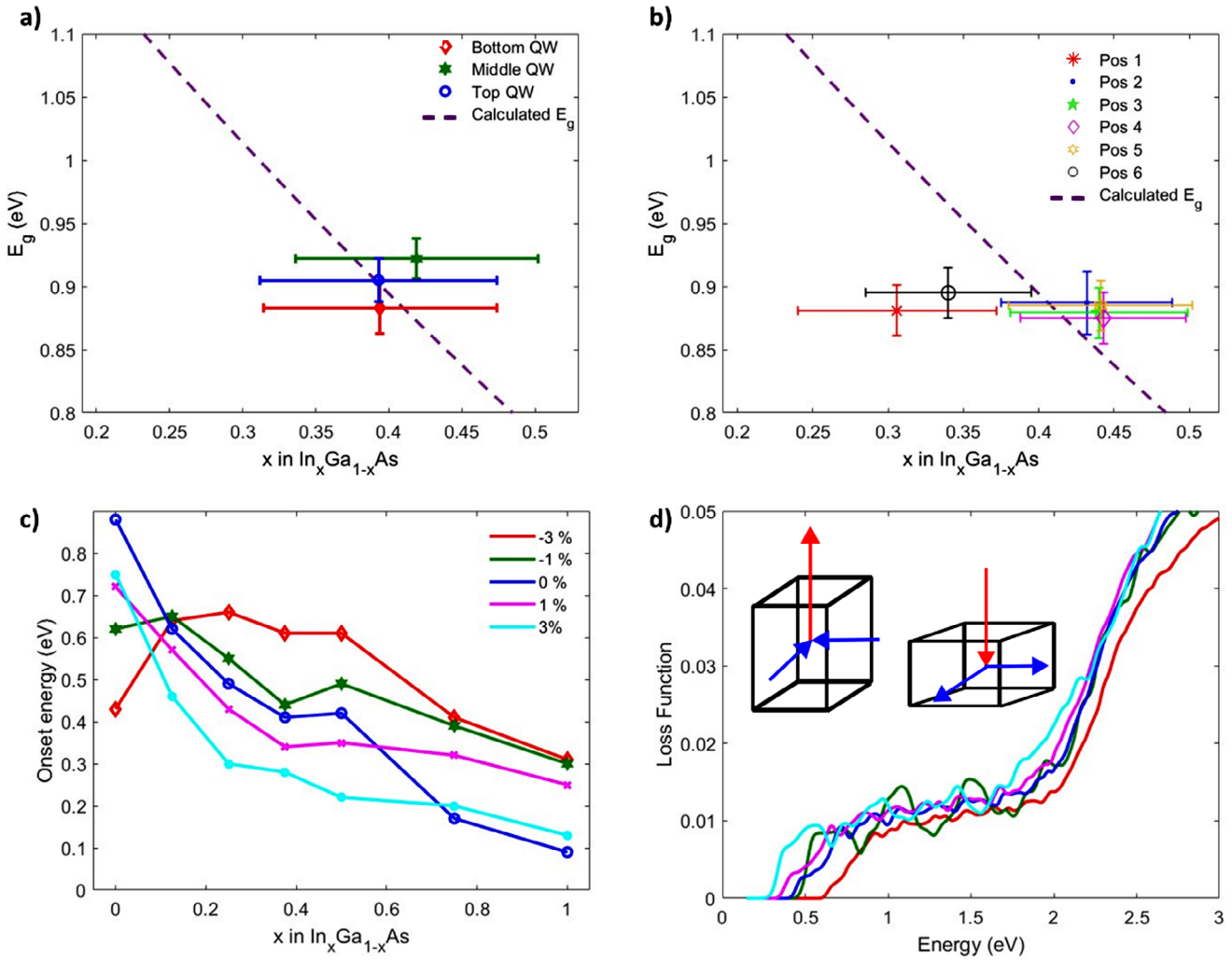

Figure 5. a) Comparison of the calculated E_g value and average measured E_g values for all QWs b) and E_g values at each position (1-6) in the bottom QW (b) as a function of In mole fraction (x). Calculated E_g as a function of x (dotted purple line) based on Equation (2), from Nahroy et al.[45] c) Simulated EELS energy onset as a function of x in $In_xGa_{1-x}As$ d) and for $In_{0.375}Ga_{0.625}As$ as a function of strain. Insert in 5d is a schematic of the uniaxial strain applied in the simulation.

Figure S16 (Supporting Information). For this composition, the energy onset is lower for high compressive strain values and shifts to higher energies for larger tensile strain values. Further highlighting that high strain magnitudes are needed to significantly affect the E_g, in agreement with previous reports,[47] and indicating that the Indium composition plays a more predominant role in the resulting E_g for a wide range of compositions and relatively low strain values. This provides a more direct correlation for the E_g variations observed between the individual QWs and within them.

While these trends provide significant insights, they suggest there may be additional factors influencing the measured E_g. This opens up exciting avenues for further investigations such as interface effects, where imperfections from the growth can lead to rough or asymmetric boundaries between layers that may induce offsets which can alter the E_g[62,63] and QW thickness effect.[5]

3. Conclusion

This study presents a comprehensive analysis of the spatially resolved E_g, chemical composition and strain across multiple $In_xGa_{1-x}As$ QWs within a metamorphic laser structure (a unique result for MOVPE, reaching telecom wavelengths), employing high-resolution STEM imaging and low-loss EELS techniques. Our findings reveal significant inhomogeneities in the In concentration and strain distribution across individual QWs, particularly near the interfaces.

The measured bandgap values ranged from 0.89 to 0.92 eV, aligning well with photoluminescence (PL) measurements (and the XRD average signal indicating fully pseudomorphic QWs).[64] However, subtle but meaningful shifts were observed within individual QWs. Notably, the local bandgap values did not fully correlate with In concentration and strain trends, suggesting that additional factors influence the E_g as measured by EELS. DFT

simulations indicate that In concentration plays a dominant role in determining the local E_g, with strain having a secondary effect, especially under low strain conditions.

These findings underscore the importance of understanding the nanoscale control over composition and strain during fabrication to optimize the optical and electronic properties of metamorphic lasers. The observed inhomogeneities could have significant implications for device performance, particularly in tuning emission wavelengths and improving efficiency. We underline that some of the variations observed are likely the consequence of complex and non-trivial cross-talking of surface organization during epitaxy, local strain build-up, and vertical strain propagation. The system here analysed comes with several challenges of its own, and significant work will be needed to improve on the current findings. Our observations, linked to the complexity of the metamorphic growth on graded structures, serve as an indication of what are the challenges ahead for future optimization.

This work also highlights the need for further investigation into nanoscale EELS measurements, which are critical for understanding high-resolution E_g mapping. Future work should focus on refining simulation models to better account for interface imperfections, as well as exploring methods to minimize local variations in composition and strain during growth.

4. Experimental Section

Sample: The $In_{0.40}Ga_{0.60}As$ QW/GaAs metamorphic laser sample was grown via metal–organic vapor phase epitaxy (MOVPE), detailed growth conditions and purity levels were reported elsewhere.[38,65] Lamellae were prepared using a TESCAN Lyra 3 dual beam Focussed Ion Beam/Scanning Electron Microscope (FIB/SEM) via conventional in situ lift out procedure.[66] Lamellae were further thinned using a Gatan Precision Ion Polishing System (PIPS) II system, followed by a final cleaning with a Fischione Model 1040 NanoMill, and baked at 125 °C overnight prior to EELS acquisition. Different lamellae were used for EDX and EELS measurements.

Electron Microscopy Techniques: Annular dark field STEM (ADF-STEM) and energy dispersive X-ray spectroscopy (EDX) were acquired with a Thermo Fisher Talos F200-X at 200 kV equipped with a four-detector in-column Super X spectrometer, offering a collection solid angle of 0.9 sr, with a dwell time of 30 ms and a pixel size of ≈0.13 nm. The lamellae used for this were ≈60 nm in thickness. For elemental quantification, Kα peaks were used to quantify Ga and As while In was quantified with the Lα peak. The background was corrected and the Brown–Powell Ionization cross-section model was used in Velox.[67] In atomic fraction (at. %) maps were generated from extracting the In at. % at each pixel in the recorded EDX dataset and applying a color map in MATLAB.

Strain mapping was carried out using the GPA plug in for Digital Micrograph from ER-C[68] on the annular bright field (ABF) and HAADF-STEM images acquired on a Nion UltraSTEM 100 electron microscope operated at 100kV. The electron optics were adjusted to a convergence angle of 30mrad and a probe size of ≈0.9 Å. BF-HAADF-STEM images with a pixel size of 0.039 nm were acquired as a rotational frame series (90° between frames), to eliminate stage drift and scanning distortions. The datasets were averaged by rigid and non-rigid registration.[69] ABF-STEM images were chosen for GPA analysis, using $In_{0.13}Ga_{0.87}As$ as the reference region and the **g** vectors $\mathbf{g} = \mathbf{004}$ and $\mathbf{g} = 2\bar{2}0$, with a mask size of 30 pixels. Theoretical strain was calculated using the formula for strain in a layer outlined in Dunstan et al.,[70] with lattice parameters derived by Vegard's law.[23]

A Nion UltraSTEM 100MC 'HERMES', fitted with a beam monochromator and cold field emission gun, was used to perform EELS and STEM imaging.[71] The operating voltage for EELS and STEM was 60kV. The electron optics were adjusted to a convergence angle of 30mrad and a probe size of ≈1.4Å. EELS spectrum images were recorded with a NION IRIS high energy resolution spectrometer equipped with a Dectris ELA hybrid pixel direct counting electron detector. The energy resolution of the experiments was ≈30meV determined by the monochromator selection slit. The collection angle of EELS was 44mrad and spectra were acquired at 5meV/channel. All raw EELS spectra were aligned and denoised using principal component analysis (PCA) before analysis,[72] as detailed in the Supporting Information.

To measure the experimental E_g, first, the zero-loss peak is removed from the three QWs by fitting a general power law model[73] before possible contributions from Cerenkov radiation were eliminated. Further details on this process are provided in Supporting Information. Once the spectrum was corrected, the QWs are divided into 6 horizontally equal-sized regions and obtain a global spectrum from each of them by summing the spectra of all the pixels in these regions. After preparing the spectrum and obtaining the 6 global spectra, an automated fitting of the direct E_g was performed:

$$I \sim A\left(E - E_g\right)^{0.5} \tag{3}$$

where I, is the intensity of the signal, A is a constant and E is Energy.[43]

Simulations: DFT simulations were performed using the CASTEP code,[74] a plane-wave and pseudopotential based implementation of DFT. The conventional cell of GaAs was used and doped with 0%, 25%, 50%, 75%, or 100% In at the Ga site, and a $2 \times 1 \times 1$ supercell was constructed to model the 12.5% and 37.5% data. After doping, the structures were geometry optimised. Under periodic boundary conditions, only the 50% and 37.5% cases have distinguishable configurations that obey the stoichiometry, and in these cases, the lowest enthalpy configuration was chosen. The plane wave basis set was converged to 1500 eV, with a Monkhorst Pack grid of $10 \times 10 \times 10$ points used throughout. This grid was optimised on the cell with the smallest real-space lattice parameters ensuring a minimum quality of calculation throughout. A $10 \times 10 \times 10$ K-point grid was used for the conventional cells, and a $5 \times 10 \times 10$ grid was used for the $2 \times 1 \times 1$ supercells. Structures were relaxed to better than an energy convergence of 2×10^{-5}eV per ion and a force convergence of 5×10^{-2}eV Å^{-1}, with a stress convergence of better than 1MPa. Strained cells were generated by taking the optimized DFT lattice parameters and applying the appropriate shift to the a and b lattice vectors to apply a biaxial strain. The system was then relaxed in a further geometry optimisation whilst the atomic positions and new a and b vectors were fixed. The recently developed meta-Generalized Gradient Approximation (GGA) functional RSCAN[75] was used to perform the simulations, ensuring a state-of-the-art treatment of the electron correlations within the system. This functional will, as a semi-local functional, show the derivative discontinuity problem that leads to the underestimation of the E_g. Finally, post-processing of the loss function was performed with the OPTADOS package[76,77] and adaptive smearing[78] of 0 .4eV.

Supporting Information

Supporting Information is available from the Wiley Online Library or from the author.

Acknowledgements

N.S. and M.A. acknowledge the support of the Engineering and Physical Sciences Research Council (Grant number EP/S023321/1). E.P. acknowledges the support of Taighde Éireann – Research Ireland under Grant Numbers 15/IA/2864, 22/FFP-A/10930 and 12/RC/2276_P2. D.K. and Q.R. acknowledge the support of SuperSTEM, the National Research Facility for Advanced Electron Microscopy funded by the Engineering and Physical Sciences Research Council (Grant number EP/W021080/1). The authors are grateful for computational support from the UK national high performance computing service, ARCHER2, for which access

was obtained via the UKCP consortium and funded by EPSRC grant ref EP/X035891/1. ICN2 acknowledges funding from Generalitat de Catalunya 2021SGR00457. This study is part of the advanced materials programme and was supported by MCIN with funding from the European Union NextGenerationEU (PRTR-C17.I1) and Generalitat de Catalunya. The authors acknowledge support from CSIC Interdisciplinary Thematic Platform (PTI +) on Quantum Technologies.

Conflict of Interest

The authors declare no conflict of interest.

Author Contributions

N.S. and M.A. conceived and planned most of the experiments. N.S. and D.K. carried out the EELS experiments, with D.K. and Q.M.R. providing support for the analysis. I.P.-H, R.L., M.B., and J.A. provided the $In_xGa_{1-x}As$ simulations and EELS correction work. A.G., E.M., and E.P provided the sample and contributed to the interpretation of the results alongside N.S. and M.A. N.S. took the lead in writing the manuscript. All authors provided critical feedback and helped shape the research, analysis, and manuscript.

Data Availability Statement

The data that support the findings of this study are available from the corresponding author upon reasonable request.

Keywords

bandgap, electron energy loss spectroscopy, in concentration, InGaAs, quantum well, strain distribution

Received: November 11, 2024
Revised: March 25, 2025
Published online:

[1] I. Tångring, S. M. Wang, M. Sadeghi, A. Larsson, X. D. Wang, *J. Cryst. Growth* **2007**, *301*, 971.
[2] M. Arai, W. Kobayashi, M. Kohtoku, *IEEE J. Sel. Top. Quantum Electron.* **2013**, *19*, 1502207.
[3] D. Wu, H. Wang, B. Wu, H. Ni, S. Huang, Y. Xiong, P. Wang, Q. Han, Z. Niu, I. Ta?ngring, S. M. Wang, *Electron. Lett.* **2008**, *44*, 474.
[4] A. Benali, P. Rajak, R. Ciancio, J. R. Plaisier, S. Heun, G. Biasiol, *J. Cryst. Growth* **2022**, *593*, 126768.
[5] I. Camps, M. Sanchez, J. C. Gonzalez, *Semicond. Sci. Technol.* **2002**, *17*, 1013.
[6] K. Takemasa, T. Munakata, M. Kobayashi, H. Wada, T. Kamijoh, *IEEE Photonics Technol. Lett.* **1998**, *10*, 495.
[7] P. J. Delfyett, in *Encyclopedia of Physical Science and Technology*, (Third Edition), (Ed: R. A. Meyers), Academic Press, New York, US **2003**.
[8] F. Bugge, U. Zeimer, H. Wenzel, R. Staske, B. Sumpf, G. Erbert, M. Weyers, G. Tränkle, *Phys. Status Solidi C* **2006**, *3*, 423.
[9] G. h. Alahyarizadeh, M. Amirhoseiny, Z. Hassan, *Int. J. Mod. Phys. B* **2015**, *29*, 1550081.
[10] D. Saxena, N. Jiang, X. Yuan, S. Mokkapati, Y. Guo, H. H. Tan, C. Jagadish, *Nano Lett.* **2016**, *16*, 5080.
[11] P. A. Chen, C. Juang, C. Y. Chang, *IEEE J. Quantum Electron.* **1993**, *29*, 2607.
[12] D. S. Sizov, R. Bhat, A. Zakharian, J. Napierala, K. Song, D. Allen, C.-E. n. Zah, *Appl. Phys. Express* **2010**, *3*, 122101.
[13] T. Uchida, H. Kurakake, H. Soda, S. Yamazaki, *Electron. Lett.* **1994**, *30*, 563.
[14] A. E. Zhukov, A. R. Kovsh, S. S. Mikhrin, E. S. Semenova, N. A. Maleev, A. P. Vasil'ev, E. V. Nikitina, N. V. Kryzhanovskaya, A. G. Gladyshev, Y. u. M. Shernyakov, Y. u. G. Musikhin, M. V. Maksimov, N. N. Ledentsov, V. M. Ustinov, Z. h. I. Alferov, *Phys. Semicond. Devices* **2003**, *37*, 1119.
[15] C. P. Kuo, S. K. Vong, R. M. Cohen, G. B. Stringfellow, *J. Appl. Phys.* **1985**, *57*, 5428.
[16] D. Shiri, Y. Kong, A. Buin, M. P. Anantram, *Appl. Phys. Lett.* **2008**, *93*, 073114.
[17] P. J. A. Thijs, L. F. Tiemeijer, J. J. M. Binsma, T. Van Dongen, *Philips J. Res.* **1995**, *49*, 187.
[18] J. Peto, G. Dobrik, G. Kukucska, P. Vancsó, A. A. Koós, J. Koltai, P. Nemes-Incze, C. Hwang, L. Tapasztó, *npj 2D Mater. Appl.* **2019**, *3*, 39.
[19] S. J. Sweeney, T. D. Eales, A. R. Adams, *J. Appl. Phys.* **2019**, *125*, 082538.
[20] M. Gal, P. J. Orders, B. F. Usher, M. J. Joyce, J. Tann, *Appl. Phys. Lett.* **1988**, *53*, 113.
[21] Y. Sun, S. E. Thompson, T. Nishida, *J. Appl. Phys.* **2007**, *101*, 104503.
[22] S. Bogusevschi, C. A. Broderick, E. P. O'Reilly, *IEEE J. Quantum Electron.* **2016**, *52*, 1.
[23] I. Vurgaftman, J. R. Meyer, L. R. Ram-Mohan, *J. Appl. Phys.* **2001**, *89*, 5815.
[24] P. Makuła, M. Pacia, W. Macyk, *J. Phys. Chem. Lett* **2018**, *9*, 6814.
[25] P. V. Sushko, S. A. Chambers, *Sci. Rep.* **2020**, *10*, 13028.
[26] M. A. Reshchikov, *J. Appl. Phys.* **2021**, *129*, 121101.
[27] R. Erni, N. D. Browning, *Ultramicroscopy* **2007**, *107*, 267.
[28] S. Martí-Sánchez, M. Botifoll, E. Oksenberg, C. Koch, C. Borja, M. C. Spadaro, V. Di Giulio, Q. Ramasse, F. J. García de Abajo, E. Joselevich, J. Arbiol, *Nat. Commun.* **2022**, *13*, 4089.
[29] O. L. Krivanek, N. Dellby, J. A. Hachtel, J.-C. Idrobo, M. T. Hotz, B. Plotkin-Swing, N. J. Bacon, A. L. Bleloch, G. J. Corbin, M. V. Hoffman, C. E. Meyer, T. C. Lovejoy, *Ultramicroscopy* **2019**, *203*, 60.
[30] W. Zhan, V. Venkatachalapathy, T. Aarholt, A. Y. u. Kuznetsov, Ø. Prytz, *Sci. Rep.* **2018**, *8*, 848.
[31] W. Zhan, C. S. Granerød, V. Venkatachalapathy, K. M. H. Johansen, I. J. T. Jensen, A. Y. u. Kuznetsov, Ø. Prytz, *Nanotechnology* **2017**, *28*, 105703.
[32] D. Keller, S. Buecheler, P. Reinhard, F. Pianezzi, D. Pohl, A. Surrey, B. Rellinghaus, R. Erni, A. N. Tiwari, *Microsc. Microanal.* **2014**, *20*, 1246.
[33] J. R. Jinschek, R. Erni, N. F. Gardner, A. Y. Kim, C. Kisielowski, *Solid State Commun.* **2006**, *137*, 230.
[34] J. Wei, T. Ogawa, B. Feng, T. Yokoi, R. Ishikawa, A. Kuwabara, K. Matsunaga, N. Shibata, Y. Ikuhara, *Nano Lett.* **2020**, *20*, 2530.
[35] A. Brokkelkamp, J. ter Hoeve, I. Postmes, S. E. van Heijst, L. Maduro, A. V. Davydov, S. Krylyuk, J. Rojo, S. Conesa-Boj, *J. Phys Chem. A* **2022**, *126*, 1255.
[36] M. Pelaez-Fernandez, Y.-C. Lin, K. Suenaga, R. Arenal, *Nanomaterials* **2021**, *11*, 3218.
[37] D. V. Beznasyuk, S. Martí-Sánchez, J.-H. Kang, R. Tanta, M. Rajpalke, T. Stankevic, A. W. Christensen, M. C. Spadaro, R. Bergamaschini, N. N. Maka, C. E. N. Petersen, D. J. Carrad, T. S. Jespersen, J. Arbiol, P. Krogstrup, *Phys. Rev. Mater.* **2022**, *6*, 034602.
[38] E. E. Mura, A. M. Gocalinska, M. O'Brien, R. Loi, G. Juska, S. T. Moroni, J. O'Callaghan, M. Arredondo, B. Corbett, E. Pelucchi, *Cryst. Growth Des.* **2021**, *21*, 2068.
[39] K.-H. Goetz, D. Bimberg, H. Jürgensen, J. Selders, A. V. Solomonov, G. F. Glinskii, M. Razeghi, *J. Appl. Phys.* **1983**, *54*, 4543.
[40] T. Fleischmann, M. Moran, M. Hopkinson, H. Meidia, G. J. Rees, A. G. Cullis, J. L. Sánchez-Rojas, I. Izpura, *J. Appl. Phys.* **2001**, *89*, 4689.

[41] T. Grieb, F. F. Krause, K. Müller-Caspary, J.-P. Ahl, M. Schowalter, O. Oppermann, J. Hertkorn, K. Engl, A. Rosenauer, *Ultramicroscopy* **2022**, *238*, 113535.
[42] D. V. Sridhara Rao, R. Sankarasubramanian, K. Muraleedharan, T. Mehrtens, A. Rosenauer, D. Banerjee, *Microsc. Microanal.* **2014**, *20*, 1262.
[43] C. S. Granerød, W. Zhan, Ø. Prytz, *Ultramicroscopy* **2018**, *184*, 39.
[44] C. A. Gadre, X. Yan, Q. Song, J. Li, L. Gu, H. Huyan, T. Aoki, S.-W. Lee, G. Chen, R. Wu, X. Pan, *Nature* **2022**, *606*, 292.
[45] R. E. Nahory, M. A. Pollack, W. D. Johnston, R. L. Barns, *Appl. Phys. Lett.* **1978**, *33*, 659.
[46] G. H. Olsen, C. J. Nuese, R. T. Smith, *J. Appl. Phys.* **1978**, *49*, 5523.
[47] B. Mondal, R. Tonner-Zech, *Phys. Scr.* **2023**, *98*, 065924.
[48] M. E. Aumer, S. F. LeBoeuf, S. M. Bedair, M. Smith, J. Y. Lin, H. X. Jiang, *Appl. Phys. Lett.* **2000**, *77*, 821.
[49] J. F. Chen, P. Y. Wang, J. S. Wang, N. C. Chen, X. J. Guo, Y. F. Chen, *J. Appl. Phys.* **2000**, *87*, 1251.
[50] J. J. P. Peters, R. Beanland, M. Alexe, J. W. Cockburn, D. G. Revin, S. Y. Zhang, A. M. Sanchez, *Ultramicroscopy* **2015**, *157*, 91.
[51] M. J. Hÿtch, E. Snoeck, R. Kilaas, *Ultramicroscopy* **1998**, *74*, 131.
[52] N. Stephen, P. Kumar, A. Gocalinska, E. Mura, D. Kepaptsoglou, Q. Ramasse, E. Pelucchi, M. Arredondo, *J. Mater. Sci.* **2023**, *58*, 9547.
[53] H. A. Fonseka, A. S. Ameruddin, P. Caroff, D. Tedeschi, M. De Luca, F. Mura, Y. Guo, M. Lysevych, F. Wang, H. H. Tan, A. Polimeni, C. Jagadish, *Nanoscale* **2017**, *9*, 13554.
[54] D. N. Quang, N. H. Tung, *Phys. Rev. B* **2008**, *77*, 125335.
[55] J. Park, S. Heo, J.-G. Chung, H. Kim, H. Lee, K. Kim, G.-S. u. Park, *Ultramicroscopy* **2009**, *109*, 1183.
[56] M. Horák, M. Stöger-Pollach, *Ultramicroscopy* **2015**, *157*, 73.
[57] P. Mori-Sánchez, A. J. Cohen, *Phys. Chem. Chem. Phys.* **2014**, *16*, 14378.
[58] J. P. Perdew, R. G. Parr, M. Levy, J. L. Balduz Jr., *Phys. Rev. Lett.* **1982**, *49*, 1691.
[59] B. Rafferty, L. M. Brown, *Phys. Rev. B* **1998**, *58*, 10326.
[60] K. Lejaeghere, G. Bihlmayer, T. Björkman, P. Blaha, S. Blügel, V. Blum, D. Caliste, I. E. Castelli, S. J. Clark, A. D. Corso, S. de Gironcoli, T. Deutsch, J. K. Dewhurst, I. D. Marco, C. Draxl, M. Dułak, O. Eriksson, J. A. Flores-Livas, K. F. Garrity, L. Genovese, P. Giannozzi, M. Giantomassi, S. Goedecker, X. Gonze, O. Grånäs, E. K. U. Gross, A. Gulans, F. Gygi, D. R. Hamann, P. J. Hasnip, *Science* **2016**, *351*, aad3000.
[61] Y. Ji, P. Lin, X. Ren, L. He, *J. Phys. Chem. A* **2022**, *126*, 5924.
[62] M. Oloumi, C. C. Matthai, *J. Phys.: Condens. Matter* **1991**, *3*, 9981.
[63] J. Tersoff, *Phys. Rev. B* **1984**, *30*, 4874.
[64] E. Mura, *Doctoral Thesis*, University College Cork, Cork, Ireland **2019**.
[65] V. Dimastrodonato, L. O. Mereni, R. J. Young, E. Pelucchi, *J. Cryst. Growth* **2011**, *315*, 119.
[66] M. Lekstrom, M. A. McLachlan, S. Husain, D. W. McComb, B. A. Shollock, *J. Phys.: Conf. Ser.* **2008**, *126*, 012028.
[67] C. J. Powell, *NIST* **1976**, *460*, 97.
[68] Geometrical phase analysis software https://er-c.org/index.php/software/stem-data-analysis/gpa/ (accessed: October 2018).
[69] L. Jones, H. Yang, T. J. Pennycook, M. S. J. Marshall, S. Van Aert, N. D. Browning, M. R. Castell, P. D. Nellist, *Adv. Struct. Chem. Imaging* **2015**, *1*, 8.
[70] D. J. Dunstan, *J. Mater. Sci.: Mater. Electron.* **1997**, *8*, 337.
[71] O. L. Krivanek, T. C. Lovejoy, M. F. Murfitt, G. Skone, P. E. Batson, N. Dellby, *J. Phys.: Conf. Ser.* **2014**, *522*, 012023.
[72] N. Bonnet, N. Brun, C. Colliex, *Ultramicroscopy* **1999**, *77*, 97.
[73] K. L. Y. Fung, M. W. Fay, S. M. Collins, D. M. Kepaptsoglou, S. T. Skowron, Q. M. Ramasse, A. N. Khlobystov, *Ultramicroscopy* **2020**, *217*, 113052.
[74] S. J. Clark, M. D. Segall, C. J. Pickard, P. J. Hasnip, M. I. J. Probert, K. Refson, M. C. Payne, *Z. Kristallographie – Cryst. Mater.* **2005**, *220*, 567.
[75] A. P. Bartók, J. R. Yates, *J. Chem. Phys.* **2019**, *150*, 161101.
[76] R. J. Nicholls, A. J. Morris, C. J. Pickard, J. R. Yates, *J. Phys.: Conf. Ser.* **2012**, *371*, 012062.
[77] A. J. Morris, R. J. Nicholls, C. J. Pickard, J. R. Yates, *Comput. Phys. Commun.* **2014**, *185*, 1477.
[78] J. R. Yates, X. Wang, D. Vanderbilt, I. Souza, *Phys. Rev. B* **2007**, *75*, 195121.